Iron adsorption on clays inferred from atomistic simulations and XAS spectroscopy

Kéri, A.; Dähn, R.; Marques Fernandes, M.; Scheinost, A.; Krack, M.; Churakov, S. V.;

Originally published:

April 2020

Environmental Science and Technology 54(2020), 11886-11893

DOI: https://doi.org/10.1021/acs.est.9b07962

Iron adsorption on clays inferred from atomistic simulations and XAS spectroscopy

Journal:	*Environmental Science & Technology*
Manuscript ID	es-2019-07962b
Manuscript Type:	Article
Date Submitted by the Author:	31-Dec-2019
Complete List of Authors:	Kéri, Annamária; Paul Scherrer Institute, Laboratory for Waste Management; University of Bern, Institute of Geological Sciences; Hungarian Academy of Sciences Centre for Energy Research, Environmental Physics Department Daehn, Rainer; Paul Scherrer Institut, Laboratory for Waste Management Marques Fernandes, Maria; Paul Scherrer Institut, Laboratory for Waste Management Scheinost, Andreas; The Rossendorf Beamline (BM20), European Synchrotron Radiation Lab Krack, Matthias; Paul Scherrer Institute, Laboratory for Scientific Computing and Modelling Churakov, Sergey; Paul Scherrer Institute, Laboratory for Waste Management; University of Bern, Institute of Geological Sciences

Iron adsorption on clays inferred from atomistic simulations and XAS spectroscopy

Annamária Kéri[1,2,3,], Rainer Dähn[1], Maria Marques Fernandez[1], Andreas Scheinost[4], Matthias Krack[5], Sergey V. Churakov[1,2,*]*

[1]Laboratory for Waste Management, Paul Scherrer Institute, CH-5232 Villigen PSI, Switzerland

[2]Institute for Geological Sciences, University of Bern, CH-3012 Bern, Switzerland

[3]Centre for Energy Research, H-1121 Budapest, Hungary

[4]The Rossendorf Beamline at the European Synchrotron Radiation Facility (ESRF), Avenue des Martyrs 71, 38043 Grenoble, France

[5]Laboratory for Scientific Computing and Modelling, Paul Scherrer Institute, CH-5232 Villigen PSI, Switzerland

*Corresponding authors' e-mail: keri.annamaria@energia.mta.hu; sergey.churakov@psi.ch

Tel: +41 56 310 4113

Fax: +41 56 310 2199

Abstract

The atomistic-level understanding of iron speciation and the probable oxidative behavior of iron $\left(Fe^{2+}_{aq} \rightarrow Fe^{3+}_{surf}\right)$ in clay minerals is fundamental for environmental geochemistry of redox reactions. Thermodynamics analysis of wet chemistry data suggests that iron adsorbs on the edge surfaces of clay minerals at distinct structural sites commonly referred as *strong*- and *weak*-sites (with high and low affinity, respectively). In this study, we applied *ab initio* molecular dynamics simulation to investigate the structure and stability of edge surfaces of *trans*- and *cis*-vacant montmorillonites. These structures were further used to evaluate the surface complexation energy and to calculate reference *ab initio* X-ray absorption spectra (XAS) for distinct inner-sphere complexes of Fe. The combination of *ab initio* simulations and XAS allowed us to reveal the Fe-complexation mechanism and to quantify the Fe partitioning between the high and low affinity sites as function of the oxidation state and loadings. Although, iron is mostly present in Fe^{3+} form, Fe^{2+} increasingly co-adsorb with increasing loadings. *Ab initio* structure relaxations of several different clay structures with substituted Fe^{2+}/Fe^{3+} in the bulk or at the surface site showed that the oxidative sorption of ferrous iron is an energetically favored process at several edge surfaces of Fe-bearing montmorillonite.

Introduction

Clay minerals are important redox agent in the global iron cycle and redox geochemistry as they contain structural and surface adsorbed iron in both ferrous and ferric forms (Fe^{2+}/Fe^{3+})[1,2]. Due to the high surface area and exceptional sorption capacity, clay minerals are widely used as hydraulic barriers for geological disposal of radioactive waste (e.g. bentonite, argillaceous rock formation)[3,4]. Structural iron in Fe-bearing clay minerals influences the surface uptake of ferrous iron[5,6], other transition[7–9] $\left(\text{e.g. } UO_2^{2+}, Tc^{7+}\right)$ and divalent[10] $\left(\text{e.g. } Zn^{2+}\right)$ ions. Wet chemistry and spectroscopic experiments show that ferrous iron competes with Zn^{2+} for the limited amount of binding sites of clay minerals[10]. At the same time, strong uptake of iron traces in excess of other divalent transition metals can be explained by the possible surface-induced oxidation of the Fe^{2+} to Fe^{3+} on clay mineral surfaces[5,6,10]. The extent of the oxidative sorption processes greatly depends on the pH, the concentration of the dissolved ferrous iron in the electrolyte as well as the oxidation state and the distribution of structural iron in the clay[5,6,10]. Despite the importance of the iron redox cycle and contaminant immobilization, the exact sorption mechanism of iron on clay minerals remain unclear[11].

The structure of smectites can be described as layers of pseudo-hexagonally ordered sheets of alumina octahedral (O) sandwiched between two siloxane tetrahedral (T) sheets (the so-called TOT-layer)[12]. Most of the Fe-bearing clay minerals belong to the 2:1 type of dioctahedral smectites in which only two thirds of the possible octahedral positions are occupied[12]. One third of the octahedral sites are *trans*-symmetric and two thirds of the octahedral sites are *cis*-symmetric with respect to the orientation of the hydroxyl (OH^-) groups[12,13]. Montmorillonite typically occurs in *cv*-vacant form having equal amount of *cis*- and *trans*-occupied sites[14]. The most stable surfaces of montmorillonite are the basal plane (001) and the (010) and (110) edges[1,15]. The sorption properties of the basal surface have comprehensively been studied by atomistic simulations[16]. The reactivity of the edge surfaces is less known because edges are difficult to isolate experimentally and the theoretical studies should rely on computationally expensive quantum mechanical simulations[16,17]. For instance, edge surfaces of montmorillonite shows high variation in reactivity because of the anisotropy of its structure[18].

Furthermore, Fe may form inner-sphere or outer-sphere complexes, which strongly depends on the ionic strength of iron in the electrolyte[19]. In the former case, the cation directly binds to the clay surface on one side and to a number of water molecules on the other side, whereas in outer-sphere hydration complexes, the interlayer cation is completely surrounded by water molecules[20]. Outer-sphere complexes are preferentially present at the basal site, while inner-

sphere complexes are formed at the edge surfaces[20]. Because of the distinct structural environment, inner- and outer-sphere complexation can be identified by spectroscopic techniques (e.g. EXAFS-, Mössbauer-spectroscopy)[19]. In the range of high to neutral pH, the sorption of Fe is strongly dominated by inner-sphere surface complexation at the edge sites[10,21,22]. The sorption measurements and spectroscopic studies indicated two distinct edge surface complexes, the so-called *strong*- $\left(\equiv S^{S}OH\right)$ and *weak-site* $\left(\equiv S^{W}OH\right)$[22,23]. Recent *ab initio* simulations demonstrate that *weak-sites* represent bidentate surface complexes attached to the octahedral sheet, whereas *strong-sites* correspond to the incorporation of ions into the edge surface terminating octahedral[24]. Although, *strong/weak-site* complexation has different structural characteristics, the exact coordination environment of the two inner-sphere complexation models is still lacking[23]. In addition, previous studies showed that the sorption of ferrous iron on clay minerals cannot satisfactory be modeled without considering the redox properties of both the structural iron and the surface complexes[5,10].

In our recent works, the structural distribution of substituting cations (e.g. amount of Fe–Fe and Mg–Fe clusters) and the preferred oxidation state of iron (Fe^{2+}/Fe^{3+} proportion) in different montmorillonites could be identified[25,26]. Furthermore, a quantitative characterization of Zn uptake processes at the water-clay interface at the atomistic level was achieved[24]. In this work, extended X-ray absorption fine structure (EXAFS) and X-ray absorption near edge structure (XANES) spectra were interpreted using *ab initio* molecular dynamics (MD) simulations based on density functional theory (DFT+U). The linear combination fit of the calculated spectra to the experimental ones allowed us to quantify the proportion of the different sorption process at different environmental conditions.

2. Materials and methods

2.1. Modelling setup

In this study, the two most common edge surfaces of montmorillonite, namely the {110} and the {010} were investigated[27]. OH^- groups were manually added to the surface to build edge surface with zero net surface charge [17,28]. The crystallographic (lattice) parameters were fixed during the simulations, while the atomic positions were relaxed. The edge surfaces of (110) and $(\bar{1}\bar{1}0)$ (Figure 1a) as well as (010) and $(0\bar{1}0)$ (Figure 1b) are not equivalent for the *cis*-vacant polymorphs of montmorillonite in contrast to *trans*-vacant phyllosilicates. To determine the energetically favored position for ferrous and ferric iron, the relaxed structures of single Fe^{2+} and Fe^{3+} ions incorporated into the octahedral sheet at different (bulk and surface)

positions were calculated for the (110), $(\bar{1}\bar{1}0)$ (010) and $(0\bar{1}0)$ edge surface models (Figure 1a,b). $2 \cdot 2 \cdot 2 \cdot 7 = 56$ distinct model structures (considering the oxidation state of iron, the orientation of the edge surfaces and *cis*/*trans*-occupational sites) were investigated. The composition of the clay platelet in these simulations was $Al_{56}Si_{112}O_{264}(OH)_{88}$. The dimensions of the orthorhombic supercell were a = 50.0 Å, b = 20.8 Å, c = 15.0 Å. Similar to previous works, the cell parameter in the a- and c-direction had larger values to reduce the interaction between the periodic images[24,25,28].

Edges of clay particles are strongly hydrophilic and covered with phys- and chem-adsorbed water molecules[19,28,29]. To have the best representation of natural conditions, the planar pores between edges were filled with water molecules to maintain the average equilibrium density of 1.0 g/ml in the middle of inter-particle space. The interlayer was free of water for the sake of computational efficiency as we primarily focused on Fe complexation at the edge sites of montmorillonite. Molecular dynamics (MD) simulations were performed for systems containing bidentate inner-sphere Fe^{2+}/Fe^{3+} complexes to the octahedral sheet at the clay edge surface including isomorphic substitution of Fe for Al in the near surface octahedral sites (Figure 2).

Two iron atoms with the same oxidation state forming *strong-like* or *weak-like* inner-sphere complexes at the either sides of the (010) and (110) edges were simulated simultaneously (Figure 2, Table 1). The total composition of the system in these simulations was $\left[Fe_x^{2+}Fe_y^{3+}Al_{38}Si_{80}O_{184}(OH)_{72} \cdot 144H_2O\right]^{x-}$ for iron at the *strong-site* and $[Al_{40}Si_{80}O_{186}(OH)_{70}]^{2-} \cdot 2\left[Fe_x^{2+}Fe_y^{3+}(OH)_2(H_2O)_2 \cdot 136H_2O\right]^{y+}$ at the *weak-site* with the stoichiometry $x = 0$ and $y = 2$ or $x = 2$ and $y = 0$, respectively. The cell parameters were fixed at a = 41.4 Å, b = 20.8 Å, c = 10.2 Å values. c-lattice parameter corresponds to a typical interlayer distance in dehydrated smectites[30], while parameter a was chosen to be large enough to minimize the interaction between periodic images across the slit pore.

2.2. *Ab initio* calculations

The structure relaxations and the molecular dynamics simulations were performed based on the density functional theory (DFT) using the Gaussian plane wave (GPW) method as it is implemented in the QUICKSTEP module of the CP2K code[31–33]. The scalar-relativistic norm-conserving pseudopotentials of Goedecker, Teter and Hutter (GTH)[34,35] were applied to avoid the explicit consideration of the core electrons. The medium-core pseudopotential of iron was composed of a [Ne] core with $3s^2\ 3p^6\ 4s^2\ 3d^6$ valance orbitals. The wave functions of the

valence electrons were described by a linear combination of contracted Gaussian-type orbitals using MOLOPT basis sets optimized for the corresponding GTH pseudopotentials[31]. All calculations were performed with a spin polarized implementation of the Perdew, Burke and Ernzerhof (PBE) exchange and correlation functional[36]. An auxiliary basis set of plane waves up to cutoff energy of 400 Ry was employed to expand the electronic density. An empirical van der Waals (vdW) correction PBE+D2 has been applied to improve the description of hydrogen bonding interaction[37]. A sufficiently strict convergence criterion ($\varepsilon_{SCF} = 3 \cdot 10^{-7}$ a. u.) for the wave function gradients during the self-consistent field (SCF) cycle was enforced ensuring a convergence of the total energy to a similar accuracy. Simulations with single iron in the (tetrahedral or octahedral) sheet were performed with a multiplicity $(2S+1)_{Fe^{2+}} = 5$ for systems with a single ferrous iron and $(2S+1)_{Fe^{3+}} = 6$ for systems with a single ferric iron, respectively. For models with two iron ions (with the same oxidation state), the multiplicity was set to $(2S+1)_{Fe^{2+}\text{—}Fe^{2+}} = (2S+1)_{Fe^{3+}\text{—}Fe^{3+}} = 1$.

Conventional DFT is known to underestimate the Coulomb repulsion between the 3*d*-electrons of iron which results in delocalized 3*d*-electrons[38]. The so-called DFT+U method was applied to improve the description of these states within the DFT formalism[39,40]. In this method, the conventional DFT equations are augmented with the so-called Hubbard term (U_{eff}), which applies an additional potential enforcing selective localization of the Fe *3d*-states. The value of U_{eff} depends on the implementation and has to be calibrated[25]. The calibration for Fe-bearing montmorillonites was performed in our previous papers[25], and was fixed for the sake of consistency at U_{eff} = 1.9 eV.

Eight system setups — representing distinct bidentate Fe complexes (*strong/weak-site*) with different oxidation state (Fe^{2+}/Fe^{3+}) at the two most relevant edge surface ((010) or (110)) sites — were pre-equilibrated with empirical force field ClayFF[41]. The equilibration was performed by classical MD simulations in the canonical ensemble (NVT) using LAMMPS package[42]. Each system was kept at 300 K with Nose-Hoover thermostat for 9 ns. Afterwards, Born-Oppenheimer *ab initio* molecular dynamics (MD) simulations were performed within the canonical (NVT) ensemble controlled by a stochastic thermostat through velocity rescaling (CSVR)[43]. The integration of the Brillouin zone was performed with Γ-point only. *Ab initio* MD simulations were performed with time step of 0.5 fs. The systems were equilibrated for 4 ps at the target temperature of 300 K followed by *ab initio* MD production runs of 16 ps duration.

2.3. Calculations of EXAFS spectra

To obtain theoretical XAS spectra, 320 molecular configurations separated by 50 fs time intervals were retrieved form molecular dynamics trajectories for each complex type. For each molecular configuration EXAFS spectra were calculated based on real space multiple scattering theory implemented in the FEFF 8.40 code[44]. Multi-scattering paths up to eight legs with path lengths up to 7.0 Å were taken into account. The scattering potential of the atoms were calculated self-consistently,[44,45] for cluster radius 5.0 Å. The amplitude reduction factor $\left(S_0^2\right)$ was set to 1.0. The default values were retained for the remaining parameters[46]. All calculated and measured spectra were normalized to the value of the first oscillation.

Reference spectra for each complex type were obtained averaging 320 individual spectra of uncorrelated molecular configurations to account for statistical and thermal disorder, accordingly. The calculated XAS spectra served as the basis for the qualitative and quantitative interpretation of the experimental data after max-min normalization. The linear combination fit of the calculated EXAFS spectra served as a basis for the quantitative interpretation of experimental ones. Quantitative comparison were performed based on the quality of the fit as it is defined in Equation 1, respectively[24,25].

$$Q_{\mathrm{EXAFS}} = \left(k^3 \sum_i \left(a_i^2 \chi_i(k)\right) - \chi^{\exp}(k)\right)^2 + \sum_i a_i^2 \rightarrow \min \qquad (1)$$

where $\chi_i(k)$ are the calculated reference spectra and $\chi^{\exp}(k)$ is the experimental EXAFS spectra, a_i^2 are the optimized fitting parameters. The term $\sum_i a_i^2$ was included following Tikhonov[47] regularization approach to avoid overfitting. The fittings were limited to the interval of EXAFS spectroscopy to $k[\mathrm{Å}^{-1}]\epsilon[3.0,9.0]$. The fit was accepted as "best fit" (Fit1) if the indicator of quality number (Q_{EXAFS}) was the lowest.

2.4. XAS experiments

The experimental XAS spectra used in this study were obtained to investigate Fe uptake mechanism on clay minerals as function of loading[48]. The EXAFS samples consisted of a synthetic iron free montmorillonite (IFM)[49,50] equilibrated for 1 week with different Fe^{2+} concentrations at pH 7 in 0.1 M NaCl. The resulting Fe loadings were 6 mmol/kg; 9 mmol/kg; 18 mmol/kg; 37 mmol/kg, respectively. Sample preparation, phase separation as well as the transfer of the wet clay pastes into the sample holders took place inside an anoxic glovebox under controlled N_2 atmosphere (O_2 < 0.1 ppm). Further preparation procedures were similar as described by Soltermann et al.[50]. Once removed from the glovebox, the samples were immediately flash-frozen in LN_2 and stored in an LN_2 dewar to prevent sample oxidation. After

transport to the Rossendorf Beamline at ESRF (Grenoble, France), the samples were individually removed from the LN_2 dewar and transferred to a closed-cycle He cryostat operating at 10 K for the XAS measurements. Measurements at <15 K protect samples from oxidation and improve signal quality by reducing thermal broadening. The XAS spectra were collected in fluorescence mode at the Fe K-edge (7112.0 eV) using a 13-element high-purity Ge solid state detector (Canberra) with digital signal analysis (XIA XMap). The polychromatic synchrotron beam was monochromatized using a pair of water-cooled Si(111) crystals, and higher-order harmonics were rejected by a Si mirror. Individual XAS scans were energy-calibrated against a simultaneously measured Fe foil, corrected for fluorescence dead time and averaged using SIXpack[51], while subsequent data reduction steps and shell fits were conducted using WinXAS[52].

3. Results and Discussion

3.1. Preferred position of Fe^{2+} and Fe^{3+} in montmorillonite

The preferred positions of Fe^{2+} and Fe^{3+} in the octahedral sheet of a clay layer were determined by comparing the total energies of the different edge surface models. First, the preferred protonation schemes for the two idealized edge surfaces were determined (Supporting Information 1). It is clearly visible that the two most relevant edge surfaces of *cis*-vacant montmorillonite $(110)/(\bar{1}\bar{1}0)$ and $(010)/(0\bar{1}0)$ edge surfaces are not related by symmetry. Ferrous and ferric iron might preferentially be incorporated into the bulk ("P2"-"P6" positions in Figure 1) or remain at the surface ("P1" and "P7" positions in Figure 1). The energies of (010) and (110) surface models with Fe^{2+} and Fe^{3+} located in "P1"-"P7" positions were calculated and plotted as function of distance to the edge surface (Figure S2 in Supporting Information 1). These raw data were crucial to correct the polarity of the surfaces as electrostatic potential difference could be imposed across the simulated clay platelet due to the asymmetric protonation. The correction procedure and the origin of the surface potential are discussed in details in Supporting Information 1. The energies of Fe^{2+} and Fe^{3+} in *cis*- and *trans*- position at different distance to the edge corrected for surface potential difference are shown in Figure 3. The energy of the *bulk-like* iron in the position "P4" is taken as the reference.

The calculated energies of Fe^{2+} and Fe^{3+} in the octahedral sheet of a montmorillonite layer and on the edge surface indicate that the oxidation of ferric iron at the surface coupled with reduction of ferrous iron in the bulk is energetically highly favored for the (110) edge surface

(Figure 3), while such a trend can not be confirmed for the (010) edge site. The energy difference between "P1" and "P7" terminated by the (110) surface suggest preferential leaching of Fe^{3+} at "P7" terminated edge and its precipitation at the "P1" terminated edge. No such energy difference is predicted for (010) edge surface as Fe incorporation energies are comparable for "P1" and "P7" positions terminated (010) surface and the bulk.

The performed *ab initio* calculations did not address the thermodynamics and kinetic of the redox reaction explicitly which depends on many environmental factors (e.g. Fe loading, pH condition and the protonation of the surface). In addition, redox-active iron may be present as *weak-site* inner-sphere complexes (Figure 2c,d) at the edge surfaces of the clay layer.

3.2. Sorption mechanism of Fe on montmorillonite edge sites

The interpretation of experimental XAS spectra based on *ab initio* modelling is a promising approach to quantify the uptake processes in minerals, which can be used to directly investigate the interplay between the metal loading and the sorption mechanism[24,25,53–55].

The *ab initio* Fe K-edge EXAFS spectra for Fe^{2+} or Fe^{3+} bidentate inner-sphere complexes at the *cis*- and *trans*-like site of the (010) and (110) edge surface representing *strong*- and *weak-site* are shown in Figure 4. The spectra for ferrous and ferric iron are clearly different. The most prominent difference is the shift in the first oscillation at $k \sim (4.10\text{-}4.25)/(4.35\text{-}4.55)$ $Å^{-1}$, and at the second oscillation at $k \sim (5.70\text{-}6.3)$ $Å^{-1}$ for ferrous iron and $k \sim (6.0\text{-}7.0)$ $Å^{-1}$ for ferric iron, respectively.

The measured EXAFS spectra of the four montmorillonite samples with increasing iron loadings from 6 mmol/kg to 37 mmol/kg looks rather similar. Detailed analysis allows, however, to reveal several sample specific features (Figure 5). The second oscillation shifts to lower k values (from $k \sim 6.6$ $Å^{-1}$ to $k \sim 6.2$ $Å^{-1}$) with increasing Fe loadings. In addition, there is a significant shape difference in the third oscillation of EXAFS spectra (double-bounced or single oscillation with right shoulder) below and above ~30 mmol/kg of iron loading. To quantify the effect of the iron loading on the uptake mechanism and to identify the preferred oxidation state of the adsorbed complexes, the measured EXAFS spectra were interpreted as a linear combination of reference spectra obtained from MD simulation of model surface complexes (Figure 5 and 6, Table S1 in Supporting Information 2).

The qualitative analysis on the liner combination fits of the experimental data to the reference *ab initio* spectra reveal clear change in the preferred oxidation state and in the uptake mechanism as function of Fe loading (Figure 5). The data analysis shows that at low loading

iron is mostly present in Fe^{3+} form at the *strong-sites*. With increasing Fe loadings, the ratio Fe^{3+}_{Ws} /Fe^{3+}_{Ss} increases indicating raising co-adsorption of Fe^{3+} on *weak-sites*. In addition, the contribution of Fe^{2+}_{Ws} shows an increasing trend with the loading suggesting an increasing competition between Fe^{2+} and Fe^{3+}. Finally, at the loading above 30 mmol/kg the contribution of Fe^{2+}_{Ss} becomes significant. The overall results indicate increasing Fe^{2+} co-adsorption at higher Fe loadings.

The observed trend in the changes of the oxidation state of the adsorbed Fe and the uptake mechanism are generally consistent with the prediction of a thermodynamic sorption model. The few differences in the theoretical fit and the experimental spectra, especially for the second and third oscillation (Figure 5c), however, are worth a discussion. These discrepancies can be explained by the relatively high background noise. The shape difference in the third oscillation of EXAFS spectra (double-bounced or single oscillation with right shoulder) below and above ~30 mmol/kg of iron loading (Figure 5c,d) could not accurately be modelled. It might indicate an increased impact of outer-sphere complexation, which was not considered in the model.

According to the thermodynamic sorption model, the total amount of Fe adsorbed on the surface should be increased by a factor of six when loading increases from 6 mmol/kg to 37 mmol/kg. Furthermore, the thermodynamic model suggests that almost all *strong-sites* are occupied by Fe at ~6 mmol/kg (Figure 6 and Table S1 in Supporting Information 2). Thus, further uptake of Fe should take place on the *weak-sites*, whereas the absolute amount of total Fe adsorbed on *strong-sites* should remain constant. It would mean a relative increase of the EXAFS signal from *weak-sites* with respect to the signal due to *strong-sites*. Contrary, the modelling results suggest that the proportion of the *weak*- and *strong-site* sorption sites remains constant (~30%:70%). These discrepancies could be explained by the moderate quality of the linear combination fit.

The results of the theoretical XANES spectroscopy and their comparison with the experimental spectra are present in Supporting Information 2. The XANES spectra of ferrous and ferric iron surface complexes are rather similar for both *strong*- and *weak*-sites making the XANES linear combination fit unreasonable.

4. Discussion and conclusions

Ab initio molecular dynamics simulations were successfully applied to reveal the structure and the stability of edge surfaces of *trans*- and *cis*- vacant montmorillonites. For the first time, the surface structure and surface energies of *cis*-vacant montmorillonite were analyzed in details. The molecular configurations from MD simulations used to obtain reference XAS spectra for

distinct Fe inner-sphere complexes on the edge of montmorillonite. The combination of *ab initio* simulations and XAS allowed us to reveal the iron complexation mechanism and its partitioning between high and low affinity sorption sites depending on the oxidation state and loading. The quantitative interpretation of the atomistic modelling based XAS spectra measured on samples with different Fe loadings indicated a particularly complex behavior of iron. Iron is mostly present in Fe^{3+} form, although, its extent decreases at increasing Fe loadings.

Calculated energy of Fe^{2+}/Fe^{3+} incorporation into different octahedral sites confirm that the oxidative sorption of Fe^{2+} at the most relevant edge surface of montmorillonite is an energetically favored process. Rosso et al. demonstrated similar oxidative sorption processes takes place at the edge surface of iron-oxides (e.g. hematite[56]), clay minerals (e.g. nontronite[57]) and micas[58] with high Fe-content. Furthermore, they calculated the kinetics of the of charge transport in the different minerals[57,59,60]. The interplay of the different electron transfer processes as Fe^{2+}/Fe^{3+} valence interchange between nearest-neighbor iron atoms via a small polaron hopping mechanism was determined and simulated. In addition, the impact of several structural defect on the electron transfer was described.

The combination of atomistic simulations and XAS spectroscopy on samples with different Fe loading showed that the sorbed amount of iron has an impact on the efficiency on the oxidative iron uptake. At higher Fe loading, larger quantities of ferrous iron remain in this oxidation state, since all possible electron donors are consumed. It explains that although *strong-site* Fe^{3+} complexes are present in the highest amount at the edge surface site, its extent is decreasing. In this study, iron free montmorillonite (IFM) without structural Fe^{3+} was investigated, which give rise to speculation about the possible electron donor. As no Fe^{3+} is present in the clay lattice of IFM, other reactive surface sites on IFM might induce the electron transfer between sorbed Fe^{2+} species and the clay particles[50,61]. The process may play a crucial role in the long-term mineralogical alteration of smectites into non-swelling phyllosilicates that are challenging to study experimentally. Future studies should aim a more complete description including the Fe^{2+}/clay redox cycle and the oxidative uptake mechanisms of Fe^{2+} on montmorillonite.

Acknowledgements

The research leading to these results has received funding from the Swiss National Science Foundation (SNSF) through Project n° SNF-200021_156412 (2015-2018). The work was supported by grants from the Swiss National Supercomputing Centre (CSCS) under project ID "s620" and "psi12". The use of computer resources of the Merlin 4 Cluster, Paul Scherrer

Institute is also gratefully acknowledged. Calculations were performed also on UBELIX (http://www.id.unibe.ch/hpc), the HPC cluster at the University of Bern. The authors thank the staff of the Rossendorf Beamline at ESRF (Grenoble, France).

References

(1) Stucki, J. W. Properties and Behaviour of Iron in Clay Minerals. In *Handbook of Clay Science*; 2006; Vol. 1, pp 423–475.

(2) Stucki, J. W.; Lee, K.; Zhang, L.; Larson, R. A. Effects of Iron Oxidation State on the Surface and Structural Properties of Smectites. *Pure Appl. Chem.* **2002**, *74* (11), 2081–2094.

(3) Karnland, O.; Olsson, S.; Nilsson, U. *Technical Report TR-06-30: Mineralogy and Sealing Properties of Various Bentonites and Smectite-Rich Clay Materials*; Stockholm, Sweden, 2006.

(4) Leupin, O. X.; Birgersson, M.; Karnland, O.; Korkeakoski, P.; Sellin, P.; Mader, U.; Wersin, P. *Technical Report 14-12: Montmorillonite Stability under near-Field Conditions*; Wettingen, Switzerland, 2014; Vol. 14–12.

(5) Soltermann, D.; Marques Fernandes, M.; Baeyens, B.; Dähn, R.; Joshi, P. A.; Scheinost, A. C.; Gorski, C. A. Fe(II) Uptake on Natural Montmorillonites. I. Macroscopic and Spectroscopic Characterization. *Environ. Sci. Technol.* **2014**, *48* (15), 8688–8697.

(6) Soltermann, D.; Baeyens, B.; Bradbury, M. H.; Marques Fernandes, M. Fe(II) Uptake on Natural Montmorillonites. II. Surface Complexation Modeling. *Environ. Sci. Technol.* **2014**, *48* (15), 8698–8705.

(7) Skomurski, F. N.; Ilton, E. S.; Engelhard, M. H.; Arey, B. W.; Rosso, K. M. Heterogeneous Reduction of U6+ by Structural Fe2+ from Theory and Experiment. *Geochim. Cosmochim. Acta* **2011**, *75* (22), 7277–7290.

(8) Ilton, E. S.; Haiduc, A.; Moses, C. O.; Heald, S. M.; Elbert, D. C.; Veblen, D. R. Heterogeneous Reduction of Uranyl by Micas: Crystal Chemical and Solution Controls. *Geochim. Cosmochim. Acta* **2004**, *68* (11), 2417–2435.

(9) Peretyazhko, T.; Zachara, J. M.; Heald, S. M.; Jeon, B. H.; Kukkadapu, R. K.; Liu, C.; Moore, D.; Resch, C. T. Heterogeneous Reduction of Tc(VII) by Fe(II) at the Solid-Water Interface. *Geochim. Cosmochim. Acta* **2008**, *72* (6), 1521–1539.

(10) Soltermann, D.; Marques Fernandes, M.; Baeyens, B.; Miehé-Brendlé, J.; Dähn, R. Competitive Fe(II)−Zn(II) Uptake on a Synthetic Montmorillonite. *Environ. Sci. Technol.* **2013**, *48* (1), 190–198.

(11) Bleam, W. F. Atomic Theories of Phyllosilicates' Quantum Chemistry, Statistical Mechanics, Electrostatic Theory, and Crystal Chemistry. *Rev. Geophys.* **1993**, *31* (1), 51–73.

(12) Guggenheim, S.; Adams, J. M.; Bain, D. C.; Bergaya, F.; Brigatti, M. F.; Drits, V. A.; Formosso, M. L. L.; Galan, E.; Kogure, T.; Stanjek, H. Summary of Recommendations of Nomenclature Committees Relevant to Clay Mineralogy: Report of the Association Internationale Pour l'Etude Des Argiles (AIPEA) Nomenclature Committee for 2006. *Clays Clay Miner.* **2006**, *54* (6), 761–772.

(13) Drits, V. A.; McCarty, D. K.; Zviagina, B. B. Crystal-Chemical Factors Responsible for the Distribution of Octahedral Cations over Trans- and Cis-Sites in Dioctahedral 2:1 Layer Silicates. *Clays Clay Miner.* **2006**, *54* (2), 131–152.

(14) Kaufhold, S.; Kremleva, A.; Krüger, S.; Rösch, N.; Emmerich, K.; Dohrmann, R. Crystal-Chemical Composition of Dicoctahedral Smectites: An Energy-Based Assessment of Empirical Relations. *ACS Earth Sp. Chem.* **2017**, *1* (10), 629–636.

(15) Liu, X.; Meijer, E. J.; Lu, X.; Wang, R. First-Principles Molecular Dynamics Insight into Fe2+ Complexes Adsorbed on Edge Surfaces of Clay Min. *Clays Clay Miner.* **2012**, *60* (4), 341–347.

(16) Churakov, S. V.; Liu, X. Quantum-Chemical Modelling of Clay Mineral Surfaces and Clay Mineral–Surface–Adsorbate Interactions. In *Surface and Interface Chemistry of Clay Minerals*; Schoonheydt, R., Johnston, C. T., Bergaya, F., Eds.; 2018; pp 49–87.

(17) Bickmore, B. R.; Rosso, K. M.; Nagy, K. L.; Cygan, R. T.; Tadanier, C. J. *Ab Initio* Determination of Edge Surface Structures for Dioctahedral 2:1 Phyllosilicates: Implications for Acid-Base for Reactivity. *Clays Clay Miner.* **2003**, *51* (4), 359–371.

(18) Tournassat, C.; Davis, J. A.; Chiaberge, C.; Grangeon, S.; Bourg, I. C. Modeling the Acid–Base Properties of Montmorillonite Edge Surfaces. *Environ. Sci. Technol.* **2016**, *50* (24), 13436–13445.

(19) Bergaya, F.; Lagaly, G. General Introduction: Clays, Clay Minerals, and Clay Science. In *Handbook of Clay Science: Developments in Clay Science*; Bergaya, F., Theng, B. K. G., Lagaly, G., Eds.; 2006; Vol. 1, pp 1–18.

(20) Brigatti, M. F.; Galan, E.; Theng, B. K. G. Structures and Mineralogy of Clay Minerals. In *Handbook of Clay Science*; Bergaya, F., Theng, B. K. G., Lagaly, G., Eds.; Elsevier, 2006; Vol. 1, pp 19–86.

(21) Bradbury, M. H.; Baeyens, B. A Mechanistic Description of Ni and Zn Sorption on Na-Montmorillonite Part II: Modelling. *J. Contam. Hydrol.* **1997**, *27* (3–4), 223–248.

(22) Bradbury, M. H.; Baeyens, B. Modelling the Sorption of Mn(II), Co(II), Ni(II), Zn(II), Cd(II), Eu(III), Am(III), Sn(IV), Th(IV), Np(V) and U(VI) on Montmorillonite: Linear Free Energy Relationships and Estimates of Surface Binding Constants for Some Selected Heavy Metals and Actinide. *Geochim. Cosmochim. Acta* **2005**, *69* (4), 875–892.

(23) Dähn, R.; Baeyens, B.; Bradbury, M. H. Investigation of the Different Binding Edge Sites for Zn on Montmorillonite Using P-EXAFS – the Strong/Weak Site Concept in the 2SPNE SC/CE Sorption Model. *Geochim. Cosmochim. Acta* **2011**, *75* (18), 5154–5168.

(24) Churakov, S. V.; Daehn, R. Zinc Adsorption on Clays Inferred from Atomistic Simulations and EXAFS Spectroscopy. *Environ. Sci. Technol.* **2012**, *46* (11), 5713–5719.

(25) Kéri, A.; Dähn, R.; Krack, M.; Churakov, S. V. Combined XAFS Spectroscopy and *Ab Initio* Study on the Characterization of Iron Incorporation by Montmorillonite. *Environ. Sci. Technol.* **2017**, *51* (18), 10585–10594.

(26) Kéri, A.; Daehn, R.; Krack, M.; Churakov, S. V. Characterisation of Structural Iron in Smectites - an *Ab Initio* Based XAS Study. *Environ. Sci. Technol.* **2018**.

(27) Bickmore, B. R.; Bosbach, D.; Michael F. H., J.; Charlet, L.; Rufe, E. In Situ Atomic Force Microscopy Study of Hectorite and Nontronite Dissolution: Implications for Phyllosilicate Edge Surface Structures and Dissolution Mechanisms. *Am. Mineral.* **2001**, *86* (4), 411–423.

(28) Churakov, S. V. *Ab Initio* Study of Sorption on Pyrophyllite: Structure and Acidity of the Edge Sites. *J. Phys. Chem. B* **2006**, *110* (9), 4135–4146.

(29) Churakov, S. V. Structure and Dynamics of the Water Films Confined between Edges of Pyrophyllite: A First Principle Study. *Geochim. Cosmochim. Acta* **2007**, *71* (5), 1130–1144.

(30) Kraehenbuehl, F.; Stoeckli, H. F.; Brunner, F.; Kahr, G.; Mueller-Vonmoos, M. Study of the Water-Bentonite System by Vapour Adsorption, Immersion Calorimetry and X-Ray Techniques: I . Micropore Volumes and Internal Surface Areas, Following Dubinin's Theory. *Clay Miner.* **2000**, *22* (1987), 1–9.

(31) VandeVondele, J.; Hutter, J. Gaussian Basis Sets for Accurate Calculations on Molecular Systems in Gas and Condensed Phases. *J. Chem. Phys.* **2007**, *127* (11), 114105.

(32) CP2K developers group http://www.cp2k.org.

(33) VandeVondele, J.; Krack, M.; Mohamed, F.; Parrinello, M.; Chassaing, T.; Hutter, J. QUICKSTEP: Fast and Accurate Density Functional Calculations Using a Mixed Gaussian and Plane Waves Approach. *Comput. Phys. Commun.* **2005**, *167* (2), 103–128.

(34) Goedecker, S.; Teter, M.; Hutter, J. Separable Dual-Space Gaussian Pseudopotentials. *Phys. Rev. B* **1996**, *54* (3), 1703–1710.

(35) Krack, M. Pseudopotentials for H to Kr Optimized for Gradient-Corrected Exchange-Correlation Functionals. *Theor. Chem. Acc.* **2005**, *114* (1–3), 145–152.

(36) Perdew, J. P.; Burke, K.; Ernzerhof, M. Generalized Gradient Approximation Made Simple. *Phys. Rev. Lett.* **1996**, *77* (18), 3865–3868.

(37) Grimme, S. Semiempirical GGA-Type Density Functional Constructed with a Long-Range Dispersion Correction. *J. Comput. Chem.* **2006**, *27* (15), 1787–1799.

(38) Rollmann, G.; Rohrbach, A.; Entel, P.; Hafner, J. First-Principles Calculation of the Structure and Magnetic Phases of Hematite. *Phys. Rev. B - Condens. Matter Mater. Phys.* **2004**, *69* (16), 165107.

(39) Liechtenstein, A. I.; Anisimov, V. I.; Zaanen, J. Density-Functional Theory and Strong Interactions: Orbital Ordering in Mott-Hubbard Insulators. *Phys. Rev. B* **1995**, *52* (8), 5467–5471.

(40) Dudarev, S. L.; Botton, G. A.; Savrasov, S. Y.; Humphreys, C. J.; Sutton, A. P. Electron-Energy-Loss Spectra and the Structural Stability of Nickel Oxide: An LSDA+U Study. *Phys. Rev. B* **1998**, *57* (3), 1505–1509.

(41) Cygan, R. T.; Greathouse, J. A.; Heinz, H.; Kalinichev, A. G. Molecular Models and Simulations of Layered Materials. *J. Mater. Chem.* **2009**, *19* (17), 2470.

(42) http://lammps.sandia.gov/.

(43) Bussi, G.; Donadio, D.; Parrinello, M. Canonical Sampling through Velocity Rescaling. *J. Chem. Phys.* **2007**, *126*, 014101.

(44) Ankudinov, A. L.; Ravel, B.; Rehr, J. J.; Conradson, S. D. Real-Space Multiple-Scattering Calculation and Interpretation of X-Ray-Absorption near-Edge Structure. *Phys. Rev. B* **1998**, *58* (12), 7565–7576.

(45) Ankudinov, A. L.; Rehr, J. J. Theory of Solid-State Contributions to the X-Ray Elastic Scattering Amplitude. *Phys. Rev. B* **2000**, *62* (4), 2437–2445.

(46) Rehr, J. J.; Ankudinov, A.; Ravel, B. User's Guide, FEFF v.8.40. 8.40. University of Washington, Department of Physics: Seeattle, USA 2006, p 66.

(47) Tikhonov, A. N.; Goncharsky, A. V.; Stepanov, V. V.; Yagola, A. G. *Numerical Methods for the Solution of Ill-Posed Problems*; Nauka, Moscow, Russia, 1995.

(48) Baeyens, B.; Marques Fernandes, M. Adsorption of Heavy Metals Including Radionuclides. In *Developments in Clay Science*; Schoonheydt, R., Johnston, C. T., Bergaya, F., Eds.; 2018; pp 125–172.

(49) Reinholdt, M.; Miehé-Brendlé, J.; Delmotte, L.; Tuilier, M.-H.; le Dred, R.; Cortès, R.; Flank, A.-M. Fluorine Route Synthesis of Montmorillonites Containing Mg or Zn and Characterization by XRD, Thermal Analysis, MAS NMR, and EXAFS Spectroscopy. *Eur. J. Inorg. Chem.* **2001**, *2001* (11), 2831.

(50) Soltermann, D.; Marques Fernandes, M.; Baeyens, B.; Dähn, R.; Miehé-Brendlé, J.; Wehrli, B.; Bradbury, M. H. Fe(II) Sorption on a Synthetic Montmorillonite. A Combined Macroscopic and Spectroscopic Study. *Environ. Sci. Technol.* **2013**, *47* (13), 6978–6986.

(51) Webb, S. M. SIXPack a Graphical User Interface for XAS Analysis Using IFEFFIT. *Phys. Scr.* **2005**, *T115*, 1011–1014.

(52) Ressler, T. WinXAS: A Program for X-Ray Absorption Spectroscopy Data Analysis under MS-Windows. *J. Synchrotron Radiat.* **1998**, *5*, 118–122.

(53) Kéri, A.; Dähn, R.; Krack, M.; Churakov, S. V. Characterization of Structural Iron in Smectites — An *Ab Initio* Based X-Ray Absorption Spectroscopy Study. *Environ. Sci. Technol.* **2019**, *53* (12), 6877–6886.

(54) Cametti, G.; Scheinost, A. C.; Giordani, M.; Churakov, S. V. Framework Modifications and Dehydration Path of a Ag + -Modified Zeolite with STI Framework Type. *J. Phys. Chem. C* **2019**, *123* (22), 13651–13663.

(55) Cametti, G.; Scheinost, A. C.; Churakov, S. V. Structural Modifications and Thermal Stability of Cd2+-Exchanged Stellerite, a Zeolite with STI Framework Type. *J. Phys. Chem. C* **2019**, *123* (41), 25236–25245.

(56) Iordanova, N.; Dupuis, M.; Rosso, K. M. Charge Transport in Metal Oxides: A Theoretical Study of Hematite α-Fe2O3. *J. Chem. Phys.* **2005**, *122*, 144305.

(57) Alexandrov, V.; Neumann, A.; Scherer, M. M.; Rosso, K. M. Electron Exchange and Conduction in Nontronite from First-Principles. *J. Phys. Chem. C* **2013**, *117* (5), 2032–2040.

(58) Rosso, K. M.; Ilton, E. S. Charge Transport in Micas: The Kinetics of FeII/III Electron Transfer in the Octahedral Sheet. *J. Chem. Phys.* **2003**, *119* (17), 9207–9218.

(59) Rosso, K. M.; Dupuis, M. Electron Transfer in Environmental Systems: A Frontier for Theoretical Chemistry. *Theor. Chem. Acc.* **2006**, *116* (1–3), 124–136.

(60) Kerisit, S.; Rosso, K. M. Kinetic Monte Carlo Model of Charge Transport in Hematite (α-Fe2O3). *J. Chem. Phys.* **2007**, *127* (12), 124706.

(61) Géhin, A.; Grenèche, J.-M.; Tournassat, C.; Brendlé, J.; Rancourt, D. G.; Charlet, L. Reversible Surface-Sorption-Induced Electron-Transfer Oxidation of Fe(II) at Reactive Sites on a Synthetic Clay Mineral. *Geochim. Cosmochim. Acta* **2007**, *71* (4), 863–876.

497 **Table 1.** Bidentate inner-sphere Fe complexation models, associated short names and panels
498 of Figure 2 in which the corresponding model structures are.

Edge surface	Inner-sphere complexation model	Oxidation state of iron	Surface site	Short name of the model	Panel in Figure 2
(010)	*strong-site*	Fe^{2+}	*cis*-like	010cSsFe2	a)
			trans-like	010tSsFe2	
		Fe^{3+}	*cis*-like	010cSsFe3	
			trans-like	010tSsFe3	
	weak-site	Fe^{2+}	*cis*-like	010cWsFe2	b)
			trans-like	010tWsFe2	
		Fe^{3+}	*cis*-like	010cWsFe3	
			trans-like	010tWsFe3	
(110)	*strong-site*	Fe^{2+}	*cis*-like	110cSsFe2	c)
			trans-like	110tSsFe2	
		Fe^{3+}	*cis*-like	110cSsFe3	
			trans-like	110tSsFe3	
	weak-site	Fe^{2+}	*cis*-like	110cWsFe2	d)
			trans-like	110tWsFe2	
		Fe^{3+}	*cis*-like	110cWsFe3	
			trans-like	110tWsFe3	

499

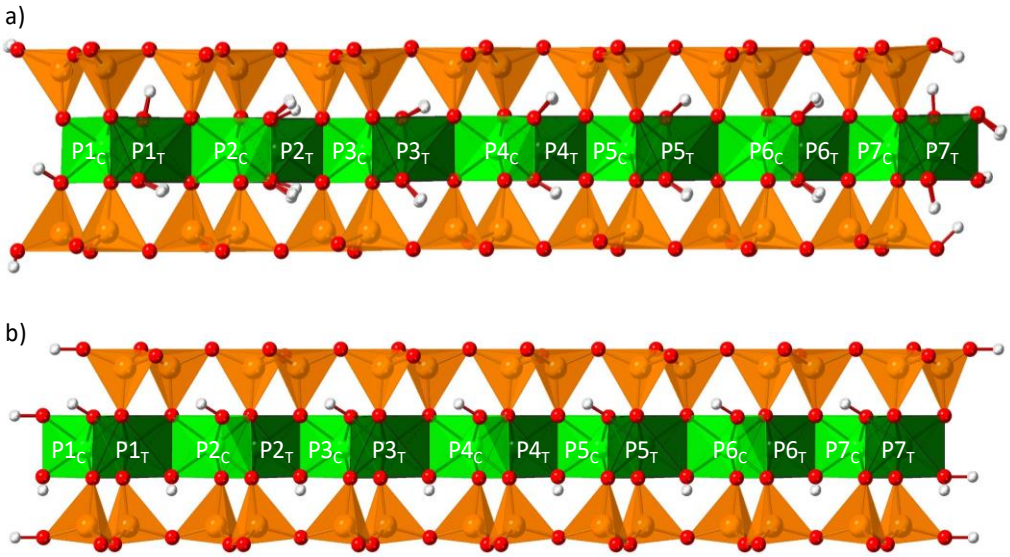

Figure 1. Views of iron substitution models. A single clay particle with (010) and (110) edge surface are shown in panels a and b, respectively. Position of iron substitution are labeled on the octahedral sheet. Alumina octahedra are shown in green, silica tetrahedra are orange, while red and grey colors correspond to oxygen and hydrogen atoms, respectively. *Cis*-octahedra are marked with light green, while dark green color corresponds to *trans*-octahedra. *Cis*- and *trans*-octahedral sites can be distinguished by the different relative position of hydroxyl (OH^-) groups. "P1" positions correspond to *cis*-like, while "P7" to *trans*-like sites.

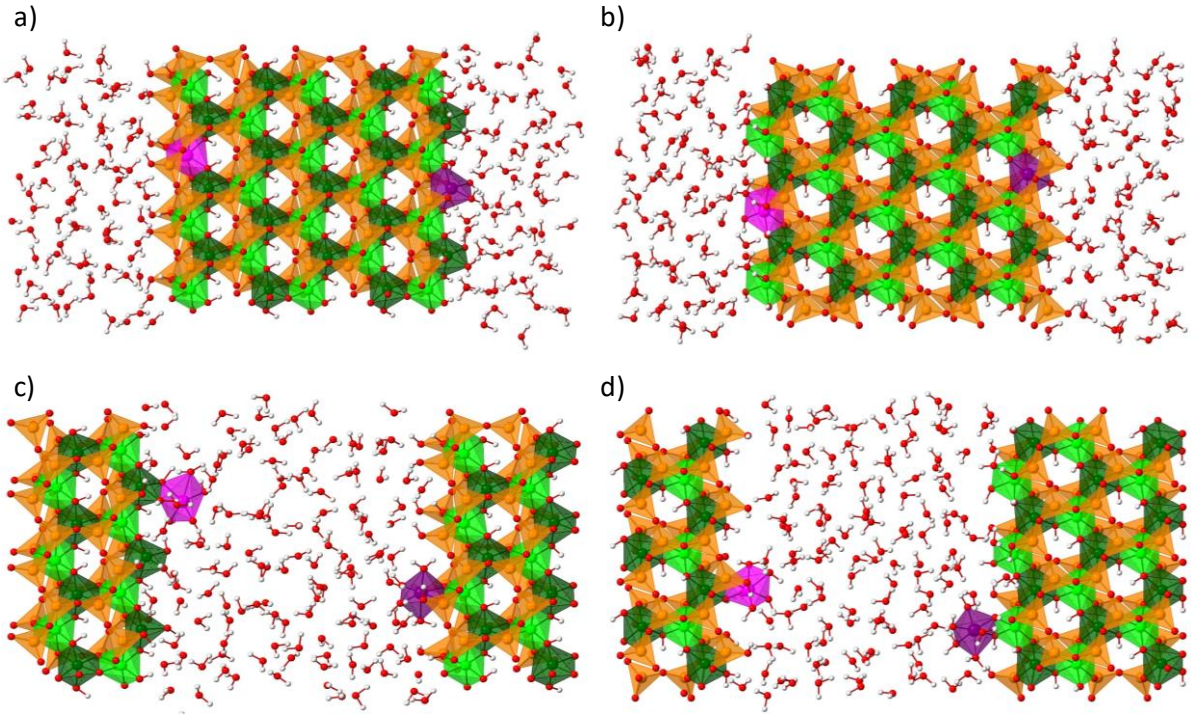

Figure 2. Views of bidentate inner-sphere sorption complexation models. The complexes referred as *strong-site* are shown in panel (a) and (b), while structures shown in panel c and d are referred as *weak-site*. In panel a and c, complexes at the (010) edge sites are shown, while view of surface complexes at the (110) edge can be seen in panel (b) and (d). Alumina octahedra are shown in green, silica tetrahedra are orange, iron is marked with pink color, while red and grey colors correspond to oxygen and hydrogen atoms, respectively. The different octahedral occupational sites can be distinguished by the different relative position of hydroxyl (OH^-) groups (*cis*-site is marked with lighter, while *trans*-site is shown with darker colors). A more detailed explanation can be found in Table 1.

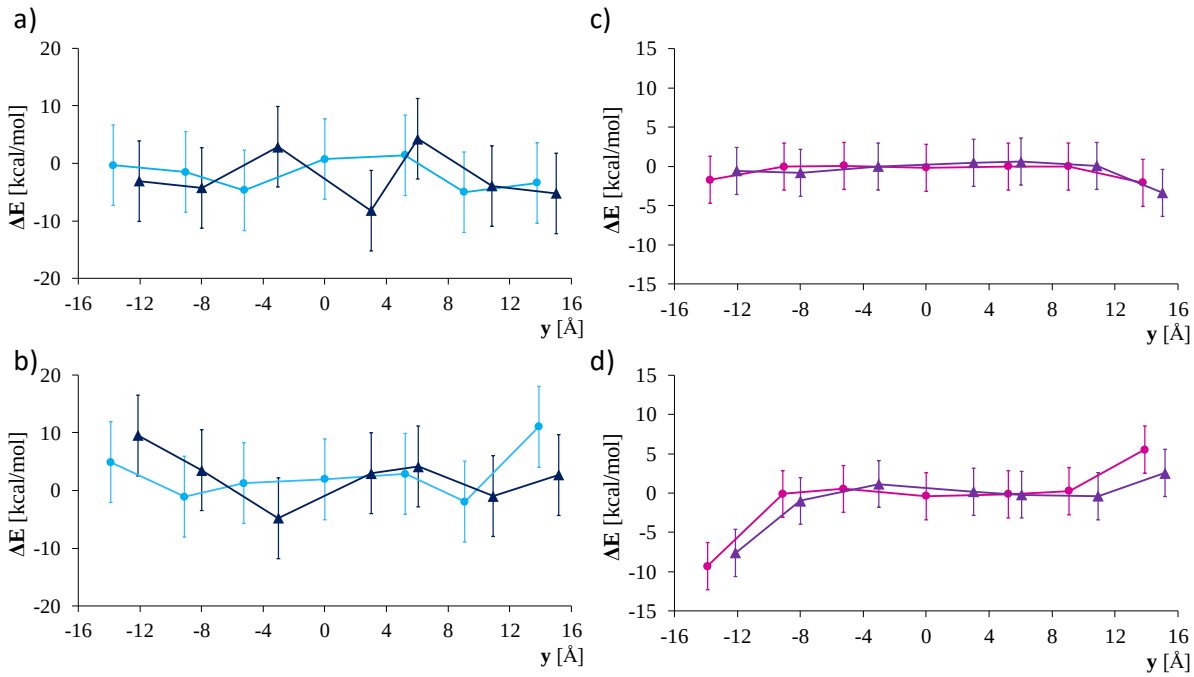

Figure 3. Relative energy for different structural position of Fe in montmorillonite structures with ferrous (panel a and b) and ferric (panel c and d) iron corrected for finite size effects, surface dipole and periodic boundary conditions (Supporting Information 1). Diagrams in panel a and c show relative energies of (010) edge sites, while diagrams in panel b and d correspond to (110) edge surface. Fe_{cis} is marked with lighter colors, while darker colors correspond to iron at the *trans*-site. Fe^{2+} and Fe^{3+} positions (e.g. "P1", "P2") are marked in Figure 1. Original energy values are plotted in Figure S2 in Supporting Information 1. The lines are drawn just to guide the eyes.

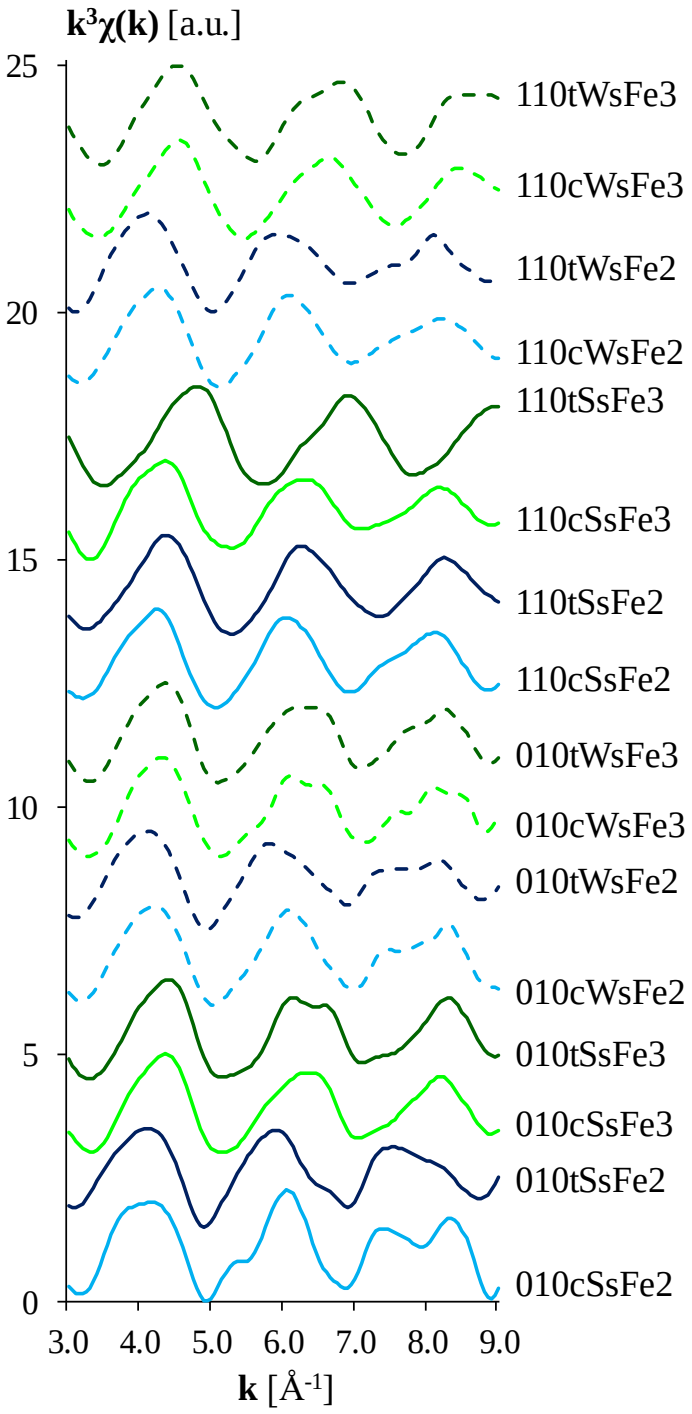

Figure 4. Theoretical EXAFS spectra of montmorillonite edge surface models representing different Fe uptake mechanisms. Blue color corresponds to Fe^{2+}, while green color indicates Fe^{3+} surface complexes. EXAFS spectra with solid lines show *strong-site*, while dashed lines represent *weak-site* complexation models. Based on the legend, a more detailed explanation can be found in Table 1.

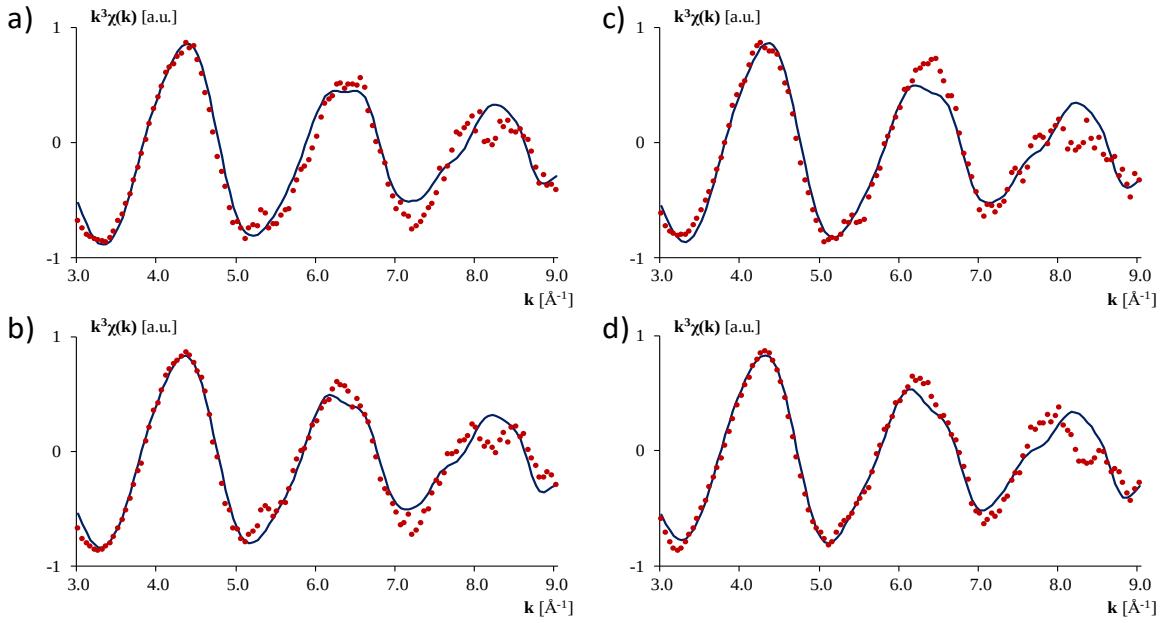

Figure 5. Experimental EXAFS spectra (red dots) and the best linear combination fits (solid lines). Contributions of individual compounds are summarized in Table S1 in Supporting Information 2. In the panels, the measured EXAFS spectra were collected from montmorillonite samples at different Fe loadings (panel a: 6 mmol/kg; panel b: 9 mmol/kg; panel c: 17 mmol/kg; panel d: 37 mmol/kg).

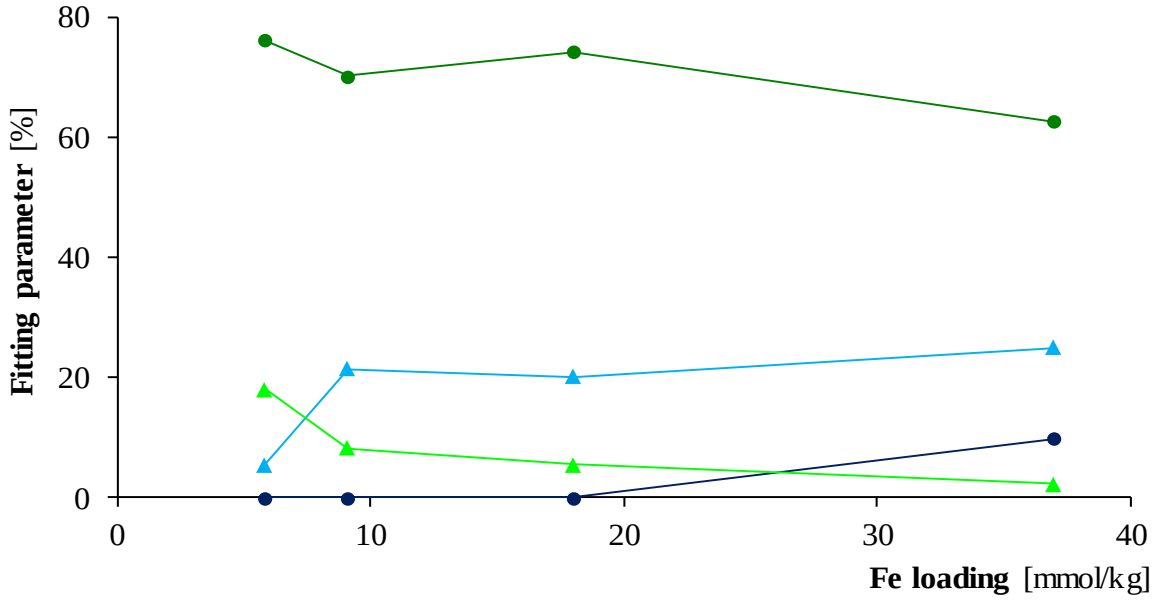

Figure 6. Contribution of the reference Fe complexes to the measured EXAFS as the function of adsorbed Fe loadings. Green colors represent Fe^{3+}, blue colors show Fe^{2+}. Darker colors and circles correspond to iron sorption on the *strong-site*, while lighter colors and triangles show sorption on *weak-site*.